

VERA Core Simulator Methodology for Pressurized Water Reactor Cycle Depletion

Brendan Kochunas, Benjamin Collins, Shane Stimpson, Robert Salko, Daniel Jabaay, Aaron Graham, Yuxuan Liu, Kang Seog Kim, William Wieselquist, Andrew Godfrey, Kevin Clarno, Scott Palmtag, Thomas Downar & Jess Gehin

To cite this article: Brendan Kochunas, Benjamin Collins, Shane Stimpson, Robert Salko, Daniel Jabaay, Aaron Graham, Yuxuan Liu, Kang Seog Kim, William Wieselquist, Andrew Godfrey, Kevin Clarno, Scott Palmtag, Thomas Downar & Jess Gehin (2017) VERA Core Simulator Methodology for Pressurized Water Reactor Cycle Depletion, Nuclear Science and Engineering, 185:1, 217-231, DOI: [10.13182/NSE16-39](https://doi.org/10.13182/NSE16-39)

To link to this article: <https://doi.org/10.13182/NSE16-39>



Published online: 08 Feb 2017.



Submit your article to this journal 



Article views: 1029



View related articles 



View Crossmark data 



Citing articles: 4 View citing articles 

VERA Core Simulator Methodology for Pressurized Water Reactor Cycle Depletion

Brendan Kochunas,^{a*} Benjamin Collins,^b Shane Stimpson,^b Robert Salko,^b Daniel Jabaay,^a Aaron Graham,^a Yuxuan Liu,^a Kang Seog Kim,^b William Wieselquist,^b Andrew Godfrey,^b Kevin Clarno,^b Scott Palmtag,^c Thomas Downar,^a and Jess Gehin^b

^a*University of Michigan, Department of Nuclear Engineering and Radiological Sciences, Ann Arbor, Michigan*

^b*Oak Ridge National Laboratory, Oak Ridge, Tennessee*

^c*Core Physics, Inc., Cary, North Carolina*

Received February 3, 2016

Accepted for Publication November 7, 2016

Abstract — This paper describes the methodology developed and implemented in the Virtual Environment for Reactor Applications Core Simulator (VERA-CS) to perform high-fidelity, pressurized water reactor (PWR), multicycle, core physics calculations. Depletion of the core with pin-resolved power and nuclide detail is a significant advance in the state of the art for reactor analysis, providing the level of detail necessary to address the problems of the U.S. Department of Energy Nuclear Reactor Simulation Hub, the Consortium for Advanced Simulation of Light Water Reactors (CASL). VERA-CS has three main components: the neutronics solver MPACT, the thermal-hydraulic (T-H) solver COBRA-TF (CTF), and the nuclide transmutation solver ORIGEN. This paper focuses on MPACT and provides an overview of the resonance self-shielding methods, macroscopic-cross-section calculation, two-dimensional/one-dimensional (2-D/1-D) transport, nuclide depletion, T-H feedback, and other supporting methods representing a minimal set of the capabilities needed to simulate high-fidelity models of a commercial nuclear reactor. Results are presented from the simulation of a model of the first cycle of Watts Bar Unit 1. The simulation is within 16 parts per million boron (ppmB) reactivity for all state points compared to cycle measurements, with an average reactivity bias of <5 ppmB for the entire cycle. Comparisons to cycle 1 flux map data are also provided, and the average 2-D root-mean-square (rms) error during cycle 1 is 1.07%. To demonstrate the multicycle capability, a state point at beginning of cycle (BOC) 2 was also simulated and compared to plant data. The comparison of the cycle 2 BOC state has a reactivity difference of +3 ppmB from measurement, and the 2-D rms of the comparison in the flux maps is 1.77%. These results provide confidence in VERA-CS's capability to perform high-fidelity calculations for practical PWR reactor problems.

Keywords — VERA, MPACT, CASL.

Note — Some figures may be in color only in the electronic version.

I. INTRODUCTION

The primary objective of the Consortium for Advanced Simulation of Light Water Reactors¹ (CASL) is to develop and deliver an enhanced nuclear reactor simulation capability. Traditional approaches to reactor analysis and design

have relied on a process using tools that are not always fully integrated or coupled, and the neutronics tools are frequently based on nodal diffusion methods that do not preserve the exact problem geometry and use approximate neutron transport physics.

For CASL to provide an enhanced simulation capability, a high-fidelity, pin-resolved radiation transport capability is required, coupled with a similar fidelity

*E-mail: bkochuna@umich.edu

physics for thermal hydraulics (T-H), fuel pin heat transfer, nuclide transmutation, and corrosion chemistry. It is also necessary for the simulation tools to be portable and efficient across a wide range of computer architectures, in particular, high-performance computing clusters. The result of this capability developed by CASL is the Virtual Environment for Reactor Applications Core Simulator (VERA-CS). VERA-CS consists of three main components: the MPACT neutronics solver,² the COBRA-TF (CTF) T-H solver,³ and the ORIGEN nuclide transmutation solver.⁴ The depletion of the core with pin-resolved power and nuclide detail with VERA-CS represents a significant advance in the state of the art for reactor analysis and provides the level of detail necessary to address the challenge problems targeted by the U.S. Department of Energy (DOE) Nuclear Reactor Simulation Hub CASL.

A recent paper by Smith and Forget⁵ on high-fidelity light water reactor (LWR) neutronics tools provides a useful perspective on the meanings of first principles and high fidelity that gives an overview of the challenges and requirements that must be met to truly claim an enhanced simulation capability. In general, an enhanced simulation tool for nuclear reactors should be able to perform isothermal calculations, zero power physics tests, reactivity worth calculations, and reactor depletion with comparisons to measured power distributions (e.g., detector responses), as well as a few other ancillary calculations. All of these requirements must be met while also modeling the fuel rods individually with minimal approximation and the other reactor support structures (e.g., grid spacers and nozzles) in as much detail as possible. In other work, the application of MPACT has been demonstrated for isothermal problems and start-up physics testing⁶ with highly resolved geometry.

This paper provides an overview of the methods in MPACT and presents results for the depletion of cycle 1 and beginning of cycle (BOC) 2 of the Watts Bar Unit 1 reactor. This work focuses on the neutronics of the core simulator capabilities and therefore emphasizes the reactor physics methods developed and implemented in the MPACT code. Section II of the paper presents the methodology for the whole-core transport calculation performed with the two-dimensional (2-D)/one-dimensional (1-D) method, and Sec. III describes the coupling of MPACT to CTF, which provides the T-H feedback. Section IV describes the depletion problem and the implementation of the ORIGEN depletion module into MPACT. Section V describes recent advances in calculating the macroscopic cross sections implemented in MPACT, and Sec. VI summarizes various supporting methodologies necessary to simulate an operational reactor over multiple

cycles. A demonstration of these capabilities for Watts Bar Unit 1 cycle 1 is provided in Sec. VII, and the paper concludes with a summary and description of future work in Sec. VIII.

II. WHOLE-CORE TRANSPORT CALCULATION METHODOLOGY

The whole-core neutron transport calculation methodology in MPACT is based on the 2-D/1-D approximation to the 3-D transport equation. The formulation of the 2-D/1-D equations is described in Sec. II.A. The approach for the discretization and solution of the resulting 2-D and 1-D equations derived in Sec. II.A are described in Secs. II.B and II.C, respectively. A more complete description of MPACT's 2-D/1-D method may be found in Ref. 7.

II.A. The 2-D/1-D Transport Method in MPACT

The 2-D/1-D approach is a numerical method for whole-core transport solutions pioneered largely by the DeCART code,⁸ though another variation was developed around the same time in the CRX code.⁹ Since then, the method has gained wider use in the reactor physics community^{10,11} and has been demonstrated to provide practical high-fidelity solutions.¹² For many practical reactor calculations, the 2-D/1-D method has become popular because its computational costs are considerably lower than those of full 3-D transport. The 2-D/1-D equations are also amenable to spatial discretization schemes that can accurately and faithfully model the physical reactor geometry. Furthermore, the 2-D/1-D equations approximate the 3-D Boltzmann equation more accurately than the conventional 3-D diffusion equation; they preserve exact transport physics in the radial directions (x and y), but they use diffusion or low-order transport physics in the axial direction (z), which is more homogeneous for most reactor applications. The key steps in the derivation of the 2-D/1-D equations begin with the steady-state 3-D multigroup (MG) transport equation:

$$\vec{\Omega} \cdot \nabla \varphi_g(\vec{r}, \vec{\Omega}) + \Sigma_{t,g}(\vec{r})\varphi_g(\vec{r}, \vec{\Omega}) = \frac{\chi_g(\vec{r})}{4\pi k_{eff}} \sum_{g'} v \Sigma_{f,g'}(\vec{r}) \int_{4\pi} \varphi_{g'}(\vec{r}, \vec{\Omega}') d\vec{\Omega}' + \sum_{g'} \int_{4\pi} \Sigma_{s,g' \rightarrow g}(\vec{r}, \vec{\Omega}' \rightarrow \vec{\Omega}) \varphi_{g'}(\vec{r}, \vec{\Omega}') d\vec{\Omega}' , \quad (1)$$

where

φ_g = angular flux

g = neutron energy group index

\vec{r}	= spatial variable
$\vec{\Omega}$	= angular variable
$\Sigma_{t,g}$	= total cross section
$\nu \Sigma_{f,g'}$	= cross section for fission multiplied with the mean neutrons produced per fission ν
$\Sigma_{s,g' \rightarrow g}$	= scattering cross section from group g' into group g and from angle $\vec{\Omega}'$ into angle $\vec{\Omega}$
k_{eff}	= neutron multiplication factor of the system
χ_g	= fission spectrum.

The 2-D/1-D equations are obtained from the 3-D transport equation by modifying the streaming operator. For the 2-D equation the following approximation is used:

$$\vec{\Omega} \cdot \nabla \varphi_g(\vec{r}, \vec{\Omega}) \approx \left(\Omega_x \frac{\partial \varphi_g(\vec{r}, \vec{\Omega})}{\partial x} + \Omega_y \frac{\partial \varphi_g(\vec{r}, \vec{\Omega})}{\partial y} \right) + \frac{1}{4\pi} \frac{\partial J_g^z(\vec{r})}{\partial z}, \quad (2)$$

where J^z is the net current in the z -direction. The net current has the usual definition and can be obtained from a diffusion approximation or some other lower-order transport solution. Introducing Eq. (2) into Eq. (1) and integrating over a finite domain in the z -direction yields the traditional 2-D equation of the 2-D/1-D approximation to the 3-D transport equation:

$$\left(\Omega_x \frac{\partial \varphi_{g,z}(x, y, \vec{\Omega})}{\partial x} + \Omega_y \frac{\partial \varphi_{g,z}(x, y, \vec{\Omega})}{\partial y} \right) + \Sigma_{t,g,z}(x, y) \times \varphi_{g,z}(x, y, \vec{\Omega}) = q_{g,z}(x, y, \vec{\Omega}) - L_{z,g}(x, y), \quad (3)$$

where q_g is the right side of Eq. (1) and L_z is the axial transverse leakage resulting from the integration of the axial derivative term in the streaming operator of Eq. (2). The subscript z now denotes that the quantity has been averaged over an axial slice.

To obtain the 1-D equation in the 2-D/1-D approximation, a different approximation for the streaming operator than that given by Eq. (2) is used. For the 1-D equation the following approximation is made:

$$\vec{\Omega} \cdot \nabla \varphi_g(\vec{r}, \vec{\Omega}) \approx \frac{1}{4\pi} \left(\frac{\partial J_g^x(\vec{r})}{\partial x} + \frac{\partial J_g^y(\vec{r})}{\partial y} \right) + \Omega_z \frac{\partial \varphi_g(\vec{r}, \vec{\Omega})}{\partial z}, \quad (4)$$

where J^x and J^y are the net currents in the x - and y -directions, respectively. Similar to Eq. (3), the 1-D equation is obtained by introducing Eq. (4) into Eq. (1) and integrating over finite intervals in x and y , but also includes integration over the azimuthal angular variable. This yields the 1-D equation of the 2-D/1-D approximation:

$$\frac{1}{2} \frac{\partial \varphi_{g,x,y}(z, \mu)}{\partial z} + \Sigma_{t,g,x,y}(z) \varphi_{g,x,y}(z, \mu) = q_{g,x,y}(z, \mu) - L_{x,y,g}(z, \mu), \quad (5)$$

where

$\mu = \Omega_z$ = cosine of the polar angle

x, y = subscripts that denote that the quantity has been averaged over a finite radial domain

$L_{x,y}$ = radial transverse leakage resulting from the integration of the x and y components of the streaming operator in Eq. (4).

Equations (3) and (5) are the typical 2-D/1-D equations solved in MPACT. Equations (3) and (5) are coupled through the transverse leakage terms, and they may be solved iteratively by alternating the evaluation of Eqs. (3) and (5), where the solution of Eq. (3) is used to construct the radial transverse leakage in Eq. (5), and conversely, the solution of Eq. (5) is used to construct the axial transverse leakage in Eq. (3). The details of the solution and discretization of Eqs. (3) and (5) are the focal points of Secs. II.B and II.C, respectively. For a detailed description of the overall iteration scheme, the reader is referred to Ref. 2 or Ref. 7.

II.B. The 2-D Method of Characteristics

The 2-D method of characteristics¹³ (MOC) is used to solve the highly heterogeneous radial problem in the reactor and is generally the preferred method for radial transport in 2-D/1-D because it can treat arbitrary geometry without significant approximations. The 2-D transport equation in the characteristic direction is obtained from Eq. (3) by applying the following coordinate transformation:

$$\vec{r}_r = \vec{r}_{r,0} + s \vec{\Omega}_r \Rightarrow \begin{aligned} x(s) &= x_0 + s \Omega_{r,x} \sin \theta \\ y(s) &= y_0 + s \Omega_{r,y} \sin \theta \end{aligned}, \quad (6)$$

where

$$\vec{r}_r = (x, y)$$

$$\vec{\Omega}_r = (\cos \alpha, \sin \alpha)$$

α = azimuthal angle
 θ = polar angle.

Applying this transformation yields the following differential equation for the characteristic direction s :

$$\frac{d}{ds}\varphi_{g,z}(\vec{r}_{r,0} + s\vec{\Omega}_r, \vec{\Omega}_r) + \frac{\Sigma_{t,g,z}(\vec{r}_{r,0} + s\vec{\Omega}_r, \vec{\Omega}_r)}{\sin \theta} \\ \times \varphi_{g,z}(\vec{r}_{r,0} + s\vec{\Omega}_r, \vec{\Omega}_r) = \frac{Q_{g,z}(\vec{r}_{r,0} + s\vec{\Omega}_r, \vec{\Omega}_r)}{\sin \theta}, \quad (7)$$

where the source Q is introduced to denote the right side of Eq. (3). Typical approximations to facilitate discretizing and evaluating the solution of Eq. (7) include the discrete ordinates approximation for the angular variable, an isotropic scattering approximation, and a flat source for spatial discretization. However, deriving and implementing variations of the solution with anisotropic scattering or linear sources is straightforward.

After discretization of the solution of Eq. (7), the classic MOC equations can be obtained for transmission of the angular flux along a segment k of a characteristic ray, as shown in Eq. (8):

$$\varphi_{i,m,g,k,z}^{out} = \varphi_{i,m,g,k,z}^{in} \exp\left(-\frac{\Sigma_{t,i,g,z} I_{i,m,k}}{\sin \theta_p}\right) \\ + \frac{Q_{i,g,z}}{\Sigma_{t,i,g,z}} \left(1 - \exp\left(-\frac{\Sigma_{t,i,g,z} I_{i,m,k}}{\sin \theta_p}\right)\right), \quad (8)$$

and the average angular flux along a segment of a characteristic ray can then be written as Eq. (9):

$$\bar{\varphi}_{i,m,g,k,z} = \frac{\varphi_{i,m,g,k,z}^{in} - \varphi_{i,m,g,k,z}^{out}}{\Sigma_{t,i,g,z} I_{i,m,k}} + \frac{Q_{i,g,z}}{\Sigma_{t,i,g,z}}, \quad (9)$$

where

m, p = discrete directions of the azimuthal and polar angles, respectively

i = spatial region index

l = length of a segment indexed by k .

Figure 1 illustrates the discretized MOC problem.

For reactor applications, the quantity of interest is the scalar flux, which is obtained by integrating the segment averaged angular fluxes of Eq. (9) traversing a given region. The MOC capability in MPACT is fully parallelized in space, angle, and ray, and a complete description of the algorithm is given in Ref. 14.

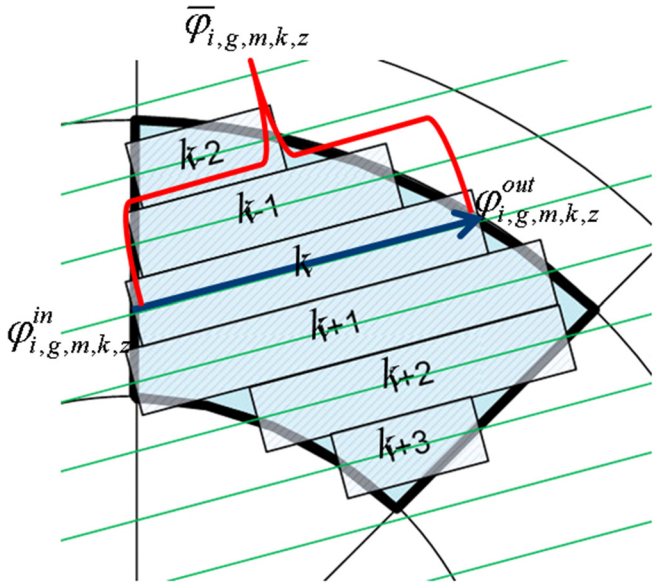


Fig. 1. Illustration of MOC discretization.

II.C. One-Dimensional Axial SP₃

The 1-D axial problem is solved to obtain the axial currents required for the transverse leakage term in the radial 2-D MOC equation. Traditionally, the 1-D calculation given by Eq. (5) is solved with the simplest yet computationally efficient diffusion approximation. However, the axial solution can also be obtained from the simplified P_N (SP_N) equations,¹⁵ in which the angular dependence of the flux [$\varphi_{g,x,y}(z, \mu)$ Eq. (5)] is approximated using an N^{th} order Legendre expansion:

$$\varphi_{g,x,y}(z, \mu) = \sum_{l=0}^{N_{mom}} \frac{2l+1}{2} \varphi_{l,g,x,y}(z) P_l(\mu), \quad (10)$$

where

l = angular moment index

z = spatial location axially

$P_l(\mu)$ = l^{th} Legendre function with respect to the polar angle

$\varphi_{l,g,x,y}(z)$ = corresponding Legendre moment of the angular flux.

Note that the diffusion approximation corresponds to $N_{mom} = 1$.

By substituting Eq. (10) into Eq. (5) and choosing $N_{mom} = 3$ and then multiplying by the corresponding Legendre polynomial and integrating over μ , results in a system of N equations can be reduced to only the even moment equations. For SP₃, the system of equations is

reduced to a system with the zeroth and second moments shown here as Eqs. (11) and (12):

$$\begin{aligned} & -\frac{4D_{0,g,x,y}}{h^2} \frac{d^2}{d\xi^2} \Phi_{0,g}(\xi) + (\Sigma_{t,g,x,y} - \Sigma_{s0,g \rightarrow g,x,y}) \Phi_{0,g}(\xi) \\ & = Q_{g,x,y}(\xi) + 2(\Sigma_{t,g,x,y} - \Sigma_{s0,g \rightarrow g,x,y}) \Phi_{2,g}(\xi) \end{aligned} \quad (11)$$

and

$$\begin{aligned} & -\frac{4D_{2,g,x,y}}{h^2} \frac{d^2}{d\xi^2} \Phi_{2,g}(\xi) + \left(\frac{9}{5} \Sigma_{t,g,x,y} - \frac{4}{5} \Sigma_{s0,g \rightarrow g,x,y} \right) \Phi_{2,g}(\xi) \\ & = -\frac{2}{5} (Q_{g,x,y}(\xi) + 2(\Sigma_{t,g,x,y} - \Sigma_{s0,g \rightarrow g,x,y}) \Phi_{0,g}(\xi)) , \end{aligned} \quad (12)$$

where

- ξ = nondimensionalized spatial variable defined on the interval $[-1, 1]$ over a node of height h
- $\Phi_{0,g}, \Phi_{2,g}$ = solution variables for the condensed angular moments of flux
- $Q_{g,x,y}$ = source term including scattering, fission, and leakage.

In MPACT, the spatial dependence of the SP_N solver is approximated using the Nodal Expansion Method (NEM) (Ref. 16) to define the higher-order shape of the intranode flux. In the implementation of NEM within MPACT, a quadratic expansion for the source and a quartic expansion for the scalar flux are used.

In Eqs. (11) and (12), the dependence on higher-order scattering data is approximated to be zero, and the diffusion coefficients for the zeroth ($D_{0,g,x,y}$) moment and second ($D_{2,g,x,y}$) moment are defined as

$$D_{0,g,x,y} = \frac{1}{3\Sigma_{tr,g,x,y}}$$

and

$$D_{2,g,x,y} = \frac{9}{35\Sigma_{tr,g,x,y}} . \quad (13)$$

III. THERMAL-HYDRAULIC FEEDBACK COUPLING WITH CTF

COBRA-TF is a T-H simulation code designed and developed for LWR analysis.³ CTF includes a wide range of T-H models important for LWR safety analysis.

These models include flow regime dependent two-phase wall heat transfer, interphase heat transfer and drag,

droplet breakup, and quench front tracking. CTF is based on a two-fluid three-field representation of the two-phase flow, including continuity of mass, axial and lateral momentum, and energy, by accounting for the liquid, entrained liquid drops, and vapor. This allows CTF to model the axial flow within each channel along with the cross flow between channels. CTF also includes several internal models to help facilitate the simulation of actual fuel assemblies, including spacer grid models for flow mixing and pressure loss, a pin conduction model, built-in material properties, and handling of noncondensable gas mixtures. The fuel pin model includes radial and azimuthal heat transfer and is solved for each axial control volume in the discretized model. A complete description of the methods in CTF is provided in Ref. 3. This section describes the coupling between MPACT and CTF to enable the solution of coupled neutronics and T-H LWR models at operating conditions.

In the MPACT/CTF coupling,¹⁷ MPACT receives temperatures and densities computed by CTF, computes the power densities, and then passes them to CTF. Within MPACT and CTF, the spatial discretizations are different as a result of their numerical methods, and the mapping of information (e.g., power, temperature, density) between the mesh in each code was designed to preserve the respective temperature/fluid and nuclide/neutron fields. The mesh for the coupling or solution transfer between CTF and MPACT is based on the x - y Cartesian grid formed by the pin cell geometry and the axial mesh defined by the user.

An example of the pin cell geometry in x - y is illustrated in Fig. 2. For each mesh (e.g., pin cell) in this grid, the solution variables in each code are integrated over the axial segment and transferred. Thus, quantities like power and mass are conserved between the codes for each axial pin cell region when transferring solution data between the codes. Figure 2 illustrates the pin cell averaged coupling for a 2×2 array of pin cells. In Fig. 2 on the left is an illustration of the spatial mesh used in MPACT for the 2-D MOC calculation. Each region bounded by black lines represents a discrete spatial cell in which a unique power density may be calculated. On the right of Fig. 2 is the subchannel mesh; again the black lines indicate the boundaries of discrete spatial cells within which the solution for the temperature or density has a discrete value. Figure 2 does not show the mesh used for the conduction solve in CTF, which is performed over the dark gray regions in the figure representing the solid regions in the subchannel mesh.

In Fig. 2, the symbol T refers to the temperature, ρ is the density, and q''' is the volumetric heat generation rate. The overbar notation indicates that the quantity has been averaged over a material region within the pin cell, and the subscript indicates the material region.

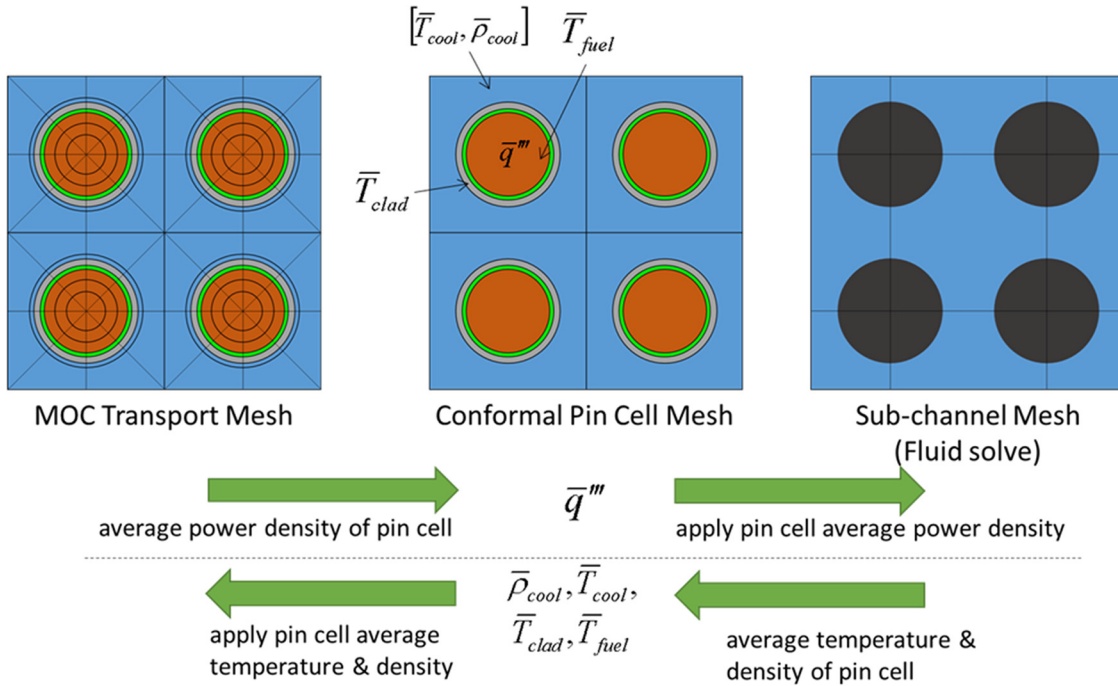


Fig. 2. Illustration of pin cell coupling model used with MPACT and CTF in VERA-CS.

COBRA-TF is a time-dependent control volume code that enforces conservation between volumes. CTF is being used within MPACT in a steady-state mode. Internally, CTF uses a pseudotransient solver to converge toward a steady-state condition for a particular flow/power state. In a coupled solve, the convergence of the approximate steady-state solution is based on five parameters: global energy, mass balance, fluid energy storage, solid energy storage, and global mass storage. For the work reported in this paper, the balance equations are converged to 10^{-6} , and the other terms are converged to 0.005%.

IV. NUCLIDE DEPLETION COUPLED WITH ORIGEN-S

The point depletion calculation in ORIGEN is used to update the fuel material compositions as the fuel is irradiated. The differential equation for the transmutation of each nuclide by radioactive decay and nuclear reaction is solved in each discrete spatial region where the composition may vary. This equation is given as

$$\frac{dN_i(t)}{dt} = \sum_{j=1} \ell_{ij} \lambda_j N_j + \bar{\Phi} \sum_{k=1} f_{ik} \sigma_{i,k} N_k - (\lambda_i + \sigma_{a,i} \bar{\Phi}) N_i , \quad (14)$$

where

$N_i(t)$ = number density of nuclide i

λ_i = radioactive disintegration constant for nuclide i

σ_a , σ_t = effective (e.g., self-shielded and energy-integrated) absorption and total cross sections, respectively

ℓ_{ij} , f_{ik} = branching ratios producing daughter nuclide j by radioactive decay or nuclide k by neutron interaction

$\bar{\Phi}$ = energy-integrated scalar flux, which is also approximated to be constant in time.

The solution of Eq. (14) is performed for MPACT by coupling with the ORIGEN code,¹ in which ORIGEN provides an application program interface, to MPACT, which enables the transfer of the MG scalar flux and microscopic cross sections from MPACT to ORIGEN and particle number densities from ORIGEN to MPACT. Several solution techniques have been implemented in ORIGEN, but in VERA-CS applications Eq. (12) is solved by the traditional matrix exponential method. The time-stepping algorithm for the depletion calculation in MPACT uses a predictor-corrector method with substepping as described in Ref. 18.

Another important detail of the coupling between MPACT and ORIGEN is that the transport-cross-section library¹⁹ does not necessarily contain data for all the fission products needed for an accurate depletion/decay calculation. As described in Sec. V, a recently developed depletion library with 244 nuclides²⁰ is used to supplement the transport library data for the depletion calculation.

However, VERA-CS may also use the full approximately 2300 nuclide chain available with ORIGEN, although for most applications this is not typically needed to obtain satisfactory results. The cross-section data for the depletion library are also not necessarily in the same group structure as the transport library, so an algorithm exists in the coupling of MPACT and ORIGEN to map the neutron energy group structure used by the transport calculation to the group structure used by ORIGEN. This improves the accuracy of the one-group cross sections in Eq. (12) since they are collapsed using the local problem dependent spectrum.

V. MACROSCOPIC-CROSS-SECTION CALCULATION

Sections III and IV described the coupling of MPACT to other physics: T-H (CTF) and depletion (ORIGEN). The coupling with the other physics produces changes to the material composition of the problem and thus modifies the macroscopic cross sections defined in the transport problem described in Sec. II. In this section, the procedure is described for computing the macroscopic cross sections in MPACT, which consists of two essential components: the MG library and the resonance self-shielding calculation.

The MG library is precomputed for use by MPACT and contains microscopic cross section and resonance integral data tabulated as a function of temperature and energy. The generation of the MPACT MG library is based on the MG AMPX library,²¹ and a number of supporting methodologies are used within the SCALE code package at the Oak Ridge National Laboratory (ORNL) to enhance the accuracy of the cross-section data.²² The latest release of the MPACT MG library includes a total of 295 isotopes and 51 energy groups, of which 22 groups (1.25 to 50,000 eV) are defined as resonance groups with resonance integral data and subgroup parameters. The resonance calculation is performed for the 22 resonance groups for a subset of 49 resonance isotopes, including the important actinides and fission products. Outside this range, base cross sections from the library (only a function of temperature) are directly used to compute the macroscopic cross section of a material region.

Three resonance self-shielding models have been implemented in MPACT: the subgroup method,^{23,24} the embedded self-shielding method^{25,26} (ESSM), and the ESSM-X method.²⁷ The subgroup method and ESSM solve the following fixed-source transport equation for each 2-D plane to model the self-shielding effects in the heterogeneous problem:

$$\vec{\Omega} \cdot \nabla \psi_g^m(\vec{r}, \vec{\Omega}) + \sum_i (\Sigma_{i,a,g}^m(\vec{r}) + \lambda_{i,g} \Sigma_{i,p}(\vec{r})) \psi_g^m(\vec{r}, \vec{\Omega}) = \frac{\Delta u_g}{4\pi} \sum_i \lambda_{i,g} \Sigma_{i,p}(\vec{r}), \quad (15)$$

where

- $\Sigma_{i,a,g}^m$ = macroscopic absorption of nuclide i
- $\Sigma_{i,p}$ = cross section of neutron potential scattering, a “billiard-ball” collision with an essentially energy-independent cross section
- $\lambda_{i,g}$ = intermediate resonance parameter.²⁸

The subgroup method solves Eq. (15) for each absorption level m (four levels in the MPACT library) in the subgroup quadrature illustrated by Fig. 3.

The scalar fluxes ϕ_g^m that result from computing the solution to Eq. (15) are used in Eq. (16) to compute the background cross section; this includes the equivalence cross section $\Sigma_{e,i,g}^m$ that accounts for the leakage effect of each resonant material region:

$$\Sigma_{i,b,g}^m = \sum_i \lambda_{i,g} \Sigma_{i,p} + \Sigma_{i,e,g}^m = \frac{\Sigma_{i,a,g}^m \phi_g^m}{\Delta u_g - \phi_g^m}. \quad (16)$$

The effective self-shielded microscopic cross sections are then obtained from the regular subgroup quadrature calculation.²⁹

In contrast to the subgroup method, ESSM solves Eq. (15) for only a single absorption level. For ESSM, the resonance integral table is directly used for cross-section interpolation once a background cross section is determined from Eq. (16). Iterations are performed between the

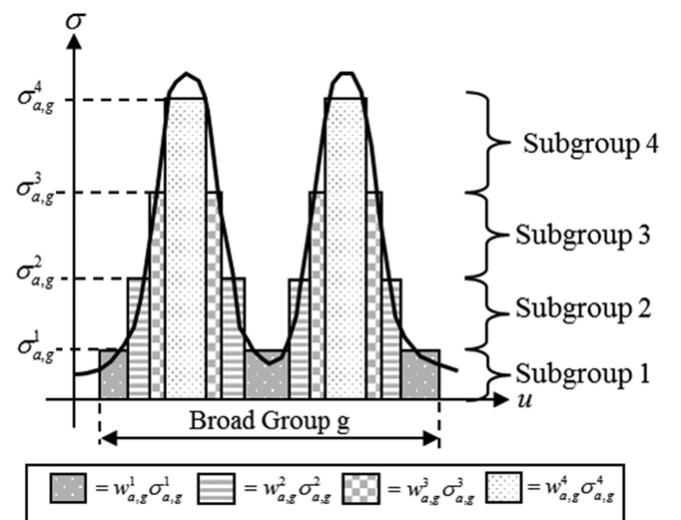


Fig. 3. Subgroup levels and weights.

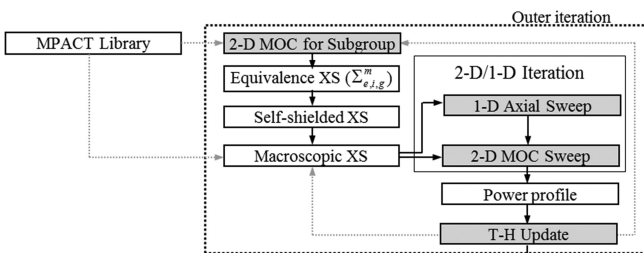


Fig. 4. Flow diagram for cross-section update.

solutions of Eqs. (15) and (16) by using the background cross section from Eq. (16) to converge the equivalence cross section and thus the effective cross section. An initial set of effective cross sections, $\Sigma_{a,i,g}^m$ in Eq. (15), can be obtained by assuming $\Sigma_{e,i,g}^m = 0$.

The ESSM-X method performs an additional quasi-1-D slowing-down calculation²⁷ to improve the accuracy of the within-pin resonance effects such as resonance interference and intrapin temperature distributions. For the latter, the MPACT code also includes an approach previously developed³⁰ and implemented in the subgroup method to correct the nonuniform temperature effect inside a fuel pin.

Figure 4 illustrates the procedure for updating the macroscopic cross sections with the subgroup method in MPACT for the coupled T-H and neutronics calculation. The subgroup fixed-source calculations are performed to update the equivalence cross section at each outer iteration after a CTF T-H update, and the macroscopic cross sections including the effective fission spectra are updated accordingly.

VI. SUPPORTING METHODOLOGIES

The simulation of a nuclear reactor requires various other capabilities and methods to accurately describe the detailed operation during the fuel burnup cycle. For example, power maneuvers are routinely conducted throughout normal operation that can involve changes to feedwater temperature, control rod position, soluble boron concentration, and a number of other reactor conditions pertinent to modeling and prediction. In MPACT, a new multistate operational capability was implemented that allows users to define a sequence of states with varying power, control rod patterns, and reactor inlet conditions to capture the operational history of a particular cycle.

VI.A. Fuel Shuffling and Restart for Multicycle Analysis

In the typical pressurized water reactor (PWR), the fuel resides in the reactor for multiple cycles, so the

capability was implemented in MPACT to relocate or shuffle the fuel from one cycle to the next and to reinsert fuel assemblies in the core that had been in the spent-fuel pool or in another reactor. Assemblies with failed rods are sometimes reconstituted, and the failed rods are replaced with dummy rods, or sometimes fresh rods are swapped into irradiated assemblies toward the normal end of life to investigate extremely high-burnup regimes. The functionality to treat all of these cases was implemented in order to ensure that MPACT would be applicable to the widest range of practical core operating conditions.

Because MPACT models each of the fuel pins explicitly with the fuel assembly, the rotation of the individual pins within the assembly must also be taken into account for models that employ symmetry. The shuffle file format uses HDF5 (Ref. 31) to facilitate portability, data compression, and input/output performance. The typical file size for the fuel composition of a single core is ~ 2 GB, so the file read and write operations support parallel execution. For the write operation, all the necessary data for a given assembly are communicated via a nonblocking gather operation, and the data are then written by a single process. The read operation has each process read the data it needs directly from the file and therefore avoids communication. This algorithm enables the composition data for a full core to be written in parallel by a few thousand processors in one or two minutes. The parallel read, which does not require data aggregation, is executed in fractions of a second for full-core calculations.

Figure 5 illustrates the shuffling feature for Watts Bar Unit 1, which is the problem presented in Sec. VII. Figure 5a shows the simulated pinwise exposures at end of cycle (EOC) 1, and Fig. 5b shows this same information shuffled to the cycle 2 location based on the pattern given in Ref. 32. The shuffling is verified by confirming that the pinwise exposures in Fig. 5b match those values in Fig. 5a for the prescribed shuffle pattern. The empty assembly locations in Fig. 5b indicate that burned fuel was not shuffled to these locations.

VI.B. Depletion of ^{10}B in Soluble Boron

The depletion of the ^{10}B isotope is different from the other isotopes because the boron is dissolved in the coolant. During the normal steady-state operation of a reactor, the ^{10}B concentration in the coolant is slowly depleted and must be modeled to be able to predict the criticality of the reactor. The ^{10}B concentration in the primary system is modeled using a simple balance equation. Assuming no source, the time rate of change of ^{10}B can be written as

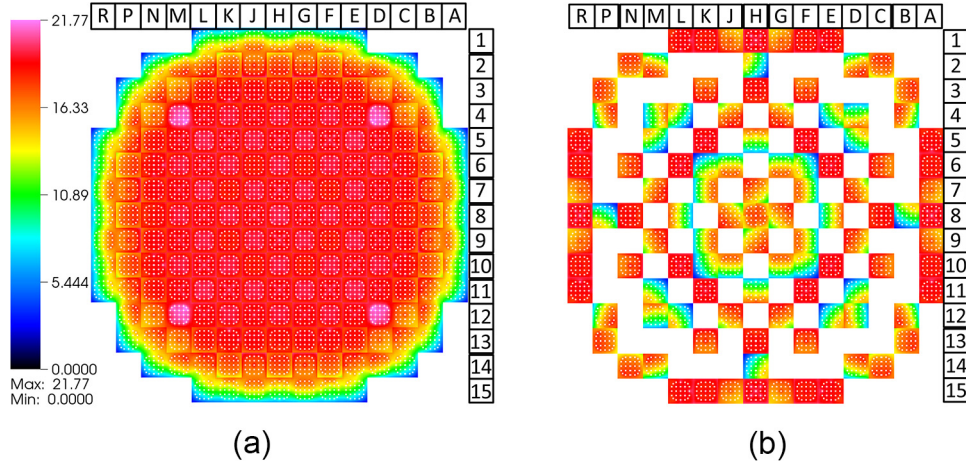


Fig. 5. (a) Watts Bar EOC 1 pinwise exposures and (b) Watts Bar BOC 2 pinwise exposures (in units of MWd/kg U).

$$\frac{dN_{^{10}B}(t)}{dt} = -N_{^{10}B}(t) \frac{\int_{V_{core}}^{\infty} \int_0^{\infty} \sigma_a^{^{10}B}(E) \phi(\vec{r}, E) dE d\vec{r}}{\int_{V_{RCS}} d\vec{r}}, \quad (17)$$

where V_{RCS} is the volume of the reactor cooling system, which is essentially the primary loop in a PWR. The solution of Eq. (17) can be written in the form of the atom fraction of ^{10}B in the soluble boron (in units of atom percent) as a function of time as shown in Eq. (18). The resulting ^{10}B number density is then obtained by multiplying the ^{10}B atom fraction with soluble boron concentration and water density:

$$C_{^{10}\text{B}}(t) [\text{at. \%}] = C_{^{10}\text{B}}(0) \frac{\exp\left(-t\alpha_{core} \sum_g \sigma_{a,g}^{^{10}\text{B}} \bar{\Phi}_g\right)}{1 - C_{^{10}\text{B}}(0) \left(1 - \exp\left(-t\alpha_{core} \sum_g \sigma_{a,g}^{^{10}\text{B}} \bar{\Phi}_g\right)\right)}, \quad (18)$$

where α_{core} is the ratio of the core coolant volume to the volume of the primary loop.

In MPACT, Eq. (18) can be used to estimate the new ^{10}B fraction in the coolant at every depletion step. The ^{10}B fraction may also be specified as part of the input to simulate the addition of new boric acid to the coolant or to better match measured conditions.

VI.C. Control Rod Decusping

When a control rod is partially inserted into an axial mesh cell or plane, the rod tip must be homogenized

within the plane since the mesh is fixed and is not adjusted to provide a discrete mesh boundary to match the material interface. If a simple volume weighting homogenization is used, the self-shielding in the control rod is underestimated, and artificially low fluxes are introduced around the control rod tip. This effect is known as control rod cusping and can result in a significant overprediction of the reactivity worth of the control rod.

To reduce the cusping effects, homogenization correction factors have been implemented in MPACT. The correction factor is unique for the control rod material. In MPACT, correction factors were developed for three control rod materials: AgInCd (AIC), B_4C , and tungsten. To obtain the correction factors for each absorber material, a 3×3 assembly case with a control rod in the center assembly was first used to quantify the rod cusping effects. The case was simulated with the control rod tip at seven positions within a plane and was also aligned with the top and bottom of the plane. It was assumed that the eigenvalue in this model should change linearly with rod position, and k_{eff} of each simulation was then compared to that of the assumed straight line and used to develop a sixth-order polynomial. In MPACT, this polynomial, which has pregenerated coefficients based on rod type, is used to adjust the volume fraction of the control rod material to minimize the reactivity error of the rod cusping effects. Figure 6 shows the reactivity as a function of the partially inserted rod position within an axial node for an AIC control rod type. Also shown are the polynomial fit to this curve and the reactivity defect with the corrected homogenization constants.

VII. WATTS BAR MULTICYCLE SIMULATION

The methods described in Secs. II through VI were used to deplete the first cycle of the Watts Bar model

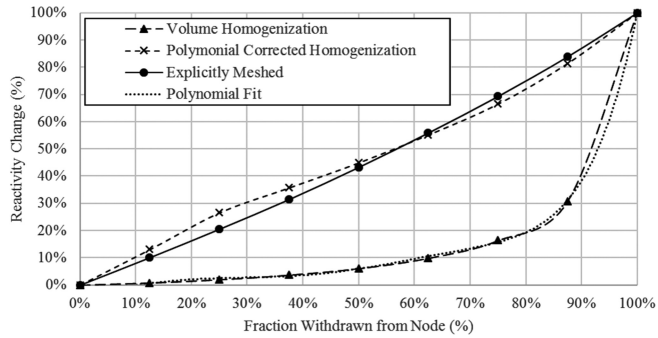


Fig. 6. Cusping treatment effect for an AIC control rod.

described in Ref. 32, which corresponds to VERA benchmark progression problem 9. The core loading pattern from cycle 1 is illustrated Fig. 7.

Because of the complexity of the actual operational history during cycle 1, an approximate power history was used as shown Table I and illustrated in Ref. 32. The approximate history preserves the integral power over the cycle and includes a ramp-up and coastdown.

For the MOC discretization in MPACT, the Chebyshev-TY quadrature³³ was used with 16 azimuthal angles per octant, 2 polar angles per octant, and a ray spacing of 0.05 cm. The axial solver used was the SP₃ kernel. A transport-corrected P₀ based on neutron leakage conservation³⁴ with the outscatter approximation was used for the scattering treatment. The cross-section library used by MPACT was a recently developed 51-group library generated by ORNL and described in detail in Ref. 35. For the T-H in CTF, the direct-moderator heating fraction was set to 2.6%. The conduction calculation was bypassed in CTF, and instead, the fuel temperatures were interpolated from a table as a function of burnup and linear heat rate given the bulk coolant temperature. The table is generated using the procedure described in Ref. 36, which utilizes the BISON fuel performance code.^{37,38} The resonance self-shielding calculation was performed at every outer

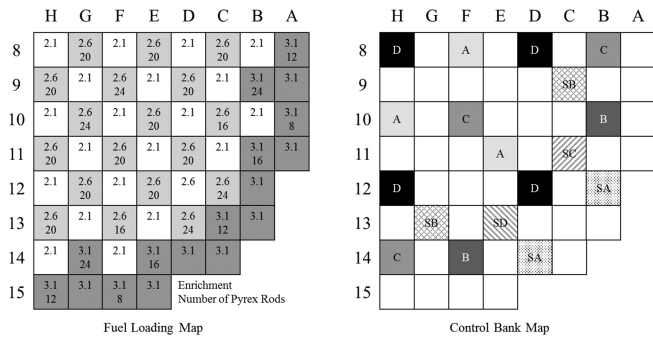
Fig. 7. Watts Bar cycle 1 public assembly, poison, and control rod layout.³²

TABLE I
Cycle 1 Simulated Operation History

Exposure (GWd/tonne)	Power (%)	Bank D	Inlet Temperature (°F)
0.000	1.00E-08	186	557.0
0.346	65.7	192	557.6
1.230	99.7	219	558.1
1.919	98	218	558.2
2.457	100	219	558.6
2.994	99.7	215	558.7
3.562	99.7	217	558.6
4.065	99.8	220	558.8
4.642	99.8	220	558.4
5.139	99.5	219	557.9
5.700	98	214	558
6.273	95.1	216	557.9
7.000	94.8	214	557.9
7.463	99.8	220	557.8
7.978	93.9	218	557.5
8.493	100.1	222	558
9.140	99.7	220	557.7
9.602	100.2	222	557.6
10.344	95.6	211	557.9
10.842	96.4	215	558.1
11.314	93.4	211	557.4
11.988	99.7	217	557.5
12.552	98	215	557.6
13.360	99.4	220	557.7
14.335	99.9	219	557.8
14.335 ^a	86.9	202	556.7
15.068	86.9	202	556.7
15.068 ^a	99.6	220	558
15.308	99.6	220	558
15.774	89.9	224	557.1
16.270	78.8	228	556.3
16.932	64.5	230	554.9

^aInstantaneous change in power.

iteration when there was a noticeable change in the temperature or coolant density distribution.

In the depletion, three substeps were used for the predictor and corrector steps between the burnup points listed in Table I, and equilibrium xenon was assumed. The control rod decusping methodology outlined in Sec. VI.C was also used. The input dimensions were also thermally expanded for the radial direction only according to the methodology in Ref. 39. In this expansion 850 K was assumed for the fuel temperature, and 585 K was assumed for all other materials.

The simulation was performed on the Falcon compute cluster, which is an SGI® ICE™ X cluster with 684 physical nodes, where each node contains two 12-core 2.5-GHz Intel Xeon E5-2680 processors with available hyperthreading and 128 GB of RAM. The problem was

decomposed in MPACT with 4088 spatial domains (56 axial and 73 radial) and 1 thread per MPI process. Of the 4088 processors used in the calculation, CTF used 292 processors (4 for each assembly). The depletion of the fuel cycle was performed using 32 state points, and the total simulation time was 22 h and 45 min. The average solve time per state was ~ 40 min.

The results for the boron letdown curve of cycle 1 are shown in Fig. 8. Reasonably good agreement with measurement is indicated, although there are still some differences. For the results shown in Fig. 8, the BOC critical boron difference is 2 parts per million boron (ppmB). The largest differences occur between 75 and 150 equivalent full-power days (EFPDs), where the Pyrex inserts are being burned out. In this range of exposures, the largest difference in critical boron concentration is 24 ppmB. Most of the remaining simulated points differ within 15 ppmB of measurement. A typical acceptance criteria PWR reactivity surveillance is 50 ppmB. Therefore, the reactivity differences within 25 ppmB shown by VERA-CS (illustrated by the right y-axis in Fig. 8) are quite good at this stage of development. Some trends are also observed in which VERA-CS generally underpredicts the critical boron compared to measurement; the average difference in critical boron concentration for the cycle is -11 ppmB.

One principal reason for the observed differences in the predicted reactivity is assumed to be the depletion of ^{10}B in the soluble boron. As far as the authors are aware, there is no measurement data of the ^{10}B concentration in cycle 1. Therefore, some engineering judgment was used to make assumptions about when the ^{10}B concentration in the soluble boron was replenished based on the other operational data available. The estimated ^{10}B concentration for cycle 1 that was developed is shown in Fig. 9 (y-axis on the left). Also shown in Fig. 9 are the differences between VERA-CS and the measured critical boron

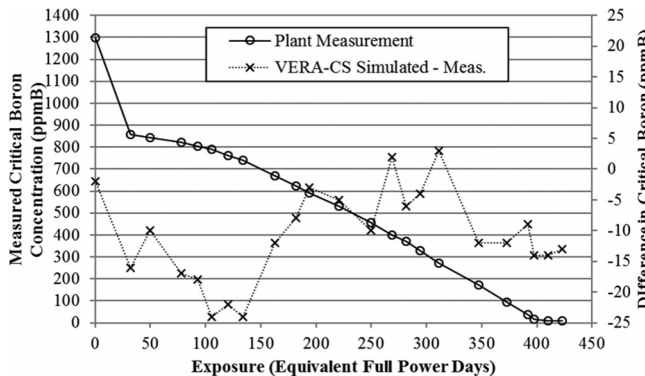


Fig. 8. Predicted critical boron concentration for Watts Bar cycle 1.

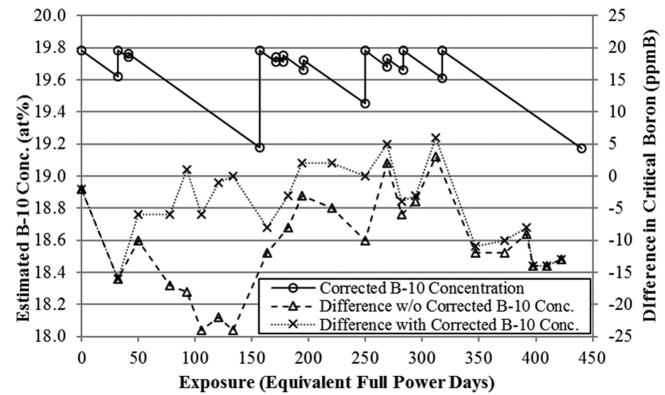


Fig. 9. Predicted critical boron concentration for Watts Bar cycle 1 with ^{10}B correction.

concentration with and without the corrected ^{10}B concentrations. The ^{10}B correction seems to improve the comparison during the 50 to 100 EFPD burnup of the core. With the corrected ^{10}B concentrations, the maximum absolute difference in the critical boron concentration is 16 ppmB, and the average difference over the cycle is <5 ppmB.

In addition to the critical boron measurements, comparisons were made to the flux maps obtained from the in-core instrumentation in the reactor. These data consist of fission chamber signal responses from detectors located in the instrument tubes in the center of various assemblies. Examples of these flux maps near BOCs 1 and 2 are shown in Figs. 10 and 11. Figure 12 shows the detailed information of what is plotted in Fig. 10 for assembly positions G-08 and C-11. Figure 13 summarizes the total differences of all measurements using a 2-D and 3-D root-mean-square (rms) of the differences.

Figures 10 and 11 show the core assembly map for the southeast quadrant of the reactor. Each assembly location in Figs. 10 and 11 includes the comparison of the predicted axial power profile with the detector response. Some assembly locations are blank, indicating that there are no measured data for these locations. Each assembly location also includes a smaller box in the upper and lower right corners. The box in the upper right gives the maximum absolute difference in the measured and predicted axial power shapes, and the lower right box includes the axial offset for that assembly location. Figures 10 and 11 also show the radially integrated detector responses to provide the core average axial power profile, as well as a summary of the 2-D axially integrated and global 3-D rms differences in the detector data. The axial offset, 2-D rms, and 3-D rms are calculated using Eqs. (19), (20), and (21), respectively:

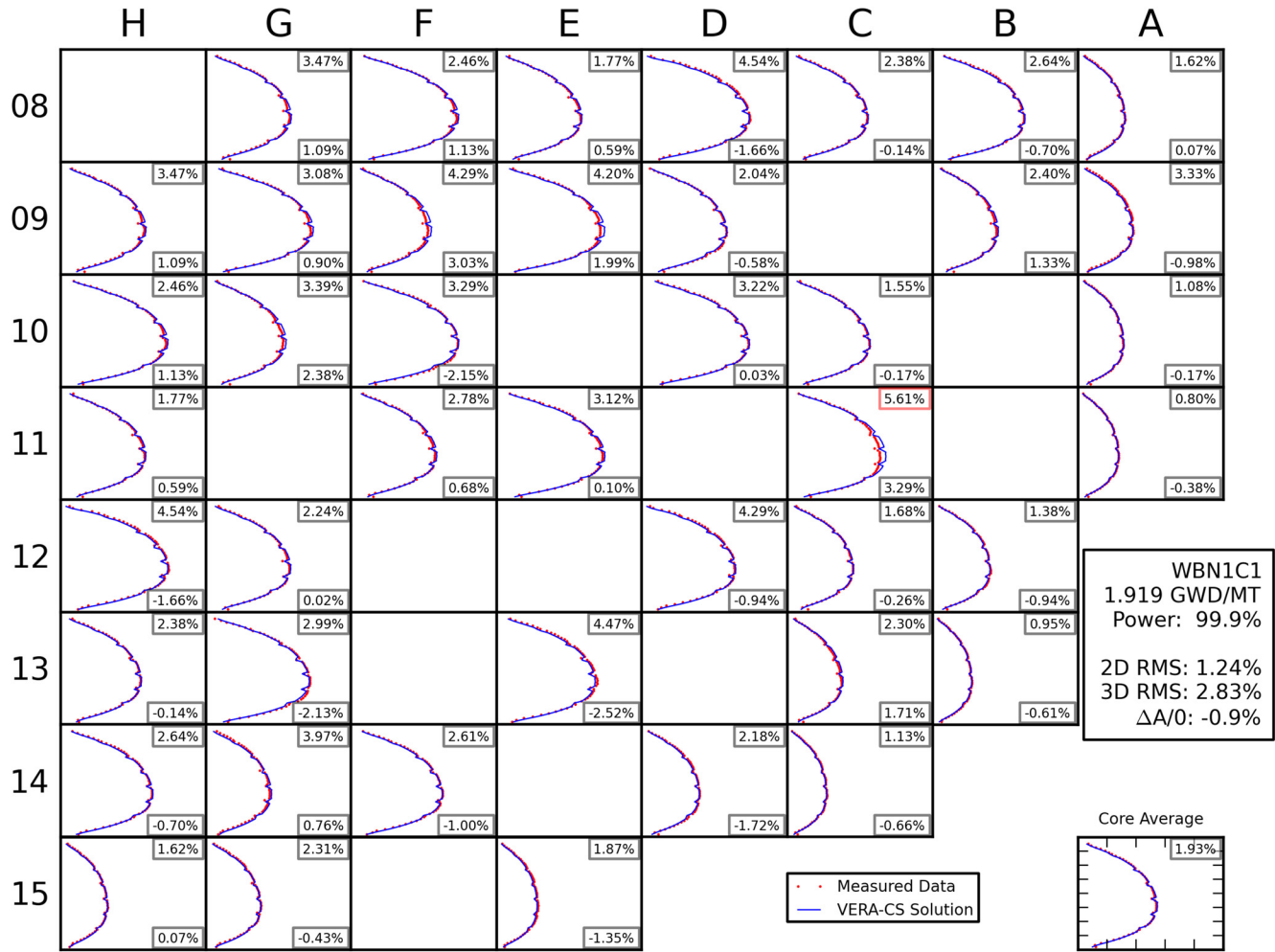


Fig. 10. Watts Bar Unit 1 BOC 1 flux map.

$$\Delta A/O =$$

$$\frac{\int_{H/2}^H \int \int P(x, y, z) dx dy dz - \int_0^{H/2} \int \int P(x, y, z) dx dy dz}{\int_{H/2}^H \int \int P(x, y, z) dx dy dz + \int_0^{H/2} \int \int P(x, y, z) dx dy dz}, \quad (19)$$

$$2\text{-D rms} = \sqrt{\frac{\sum_j \sum_i (\bar{f}_{i,j}^{\text{sim}} - \bar{f}_{i,j}^{\text{meas}})^2}{\sum_j \sum_i}}, \quad (20)$$

and

$$3\text{-D rms} = \sqrt{\frac{\sum_k \sum_j \sum_i (f_{i,j,k}^{\text{sim}} - f_{i,j,k}^{\text{meas}})^2}{\sum_k \sum_j \sum_i}}. \quad (21)$$

In Eq. (19), P is the power, and H is the height of the active core. In Eqs. (20) and (21), f represents the discretely measured and simulated quantity being compared. The subscripts i , j , and k denote the grids corresponding to the Cartesian directions x , y , and z , respectively. The \bar{f} term in Eq. (20) indicates that the quantity was first averaged over the axial (k or z) direction.

The accuracy of most of the VERA-CS results is reasonably consistent with the expected core simulator accuracies noted in Ref. 5, which indicates that the hot full power-predicted boron concentration should be within 25 ppmB of measurement, the 2-D rms at any point should be <1.5%, and the 1-D axial rms at any location should be <1 rms% compared to measured data. As was shown in Fig. 8, the VERA-CS accuracy for the core reactivity difference for the critical boron concentration is <25 ppmB for all state points compared. Furthermore, if the critical boron concentration is adjusted to correct for ^{10}B depletion, the agreement improves. As summarized in Fig. 13, the 2-D rms% is <1.5% for all depletion state

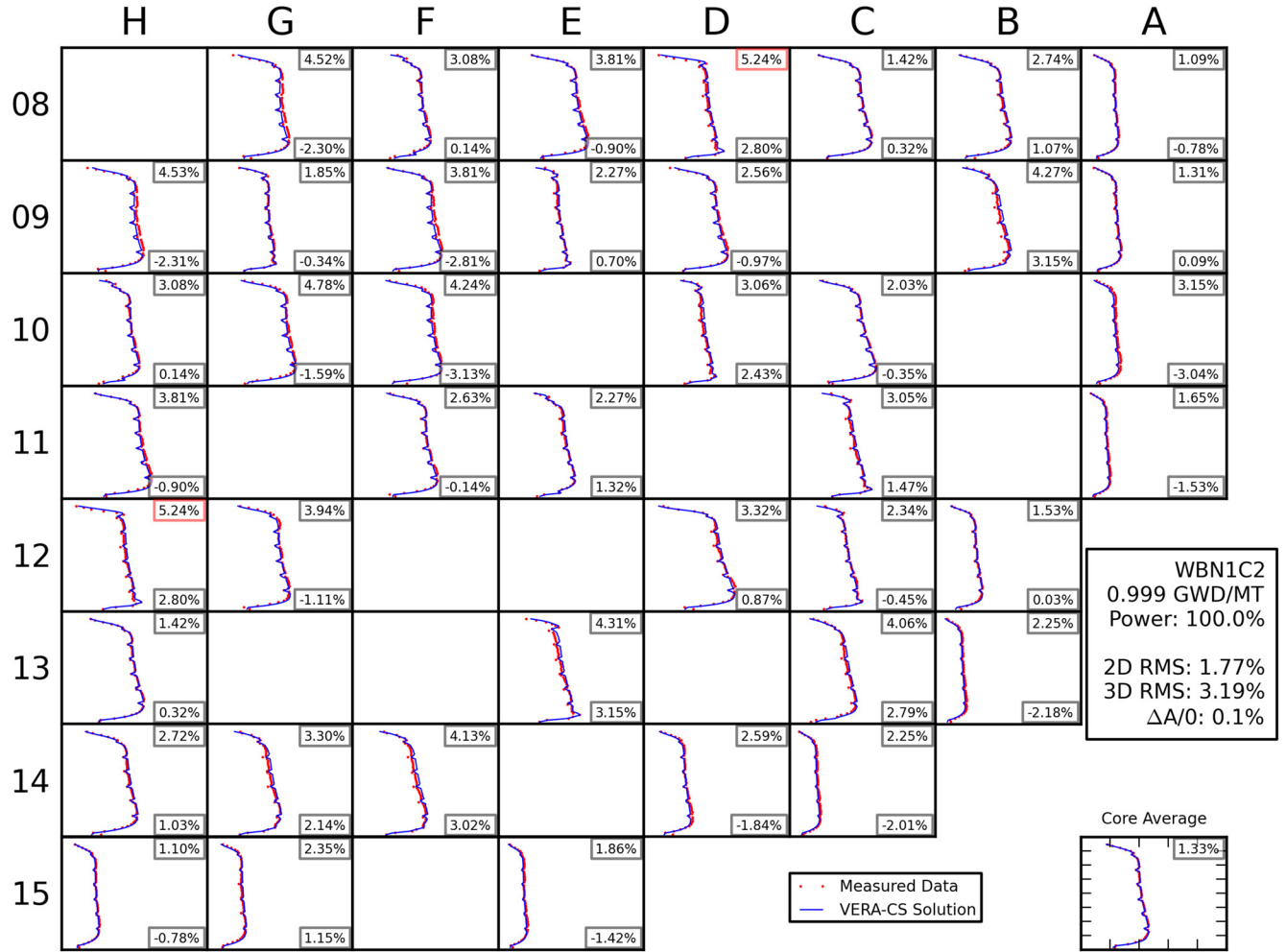


Fig. 11. Watts Bar Unit 1 BOC 2 flux map.

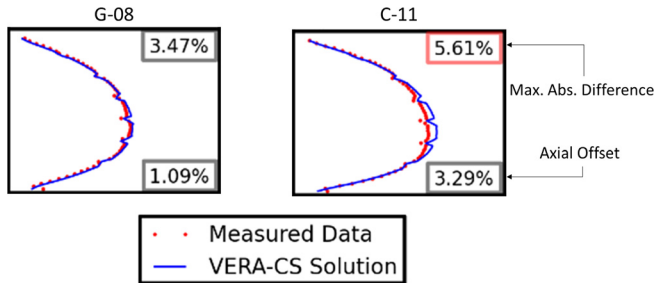


Fig. 12. Watts Bar Unit 1 cycle 1 flux maps for assemblies G-08 and C-11.

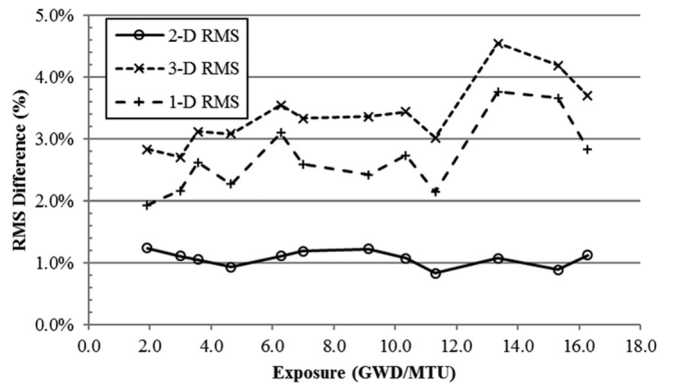


Fig. 13. VERA-CS comparisons to Watts Bar Unit 1 cycle 1 flux maps.

points. However, the 1-D axial rms% is not as close to the 1% limit recommended in Ref. 5, which suggests that there are some areas for improvement in VERA-CS.

The cycle 2 result is for the first state point at 100% power with flux map data. In the comparison of this state point, the critical boron difference is +3 ppmB, the 2-D rms% is observed to be 1.77%, and the 1-D rms% and 3-D rms% are 1.33% and 3.19%, respectively. Compared to

cycle 1, the observed difference in reactivity with measurement is similar. The 2-D rms% is slightly higher than the values observed in cycle 1, and above that suggested in Ref. 5, but the 1-D rms and 3-D rms are much improved compared to the cycle 1 data. Again, we conclude that these differences are appropriate for

this stage of development and, while good, do have room for improvement.

VIII. CONCLUSIONS

This paper summarizes development of a new high-fidelity reactor depletion code VERA-CS. The depletion of the core for multiple cycles with pin-resolved power and nuclide detail represents a significant advance in the state of art for reactor analysis and provides the level of detail necessary to address the challenging problems being addressed within the DOE Nuclear Reactor Simulation Hub CASL. An overview is presented of the methodology in VERA-CS that enables the high-fidelity simulation of a PWR through multiple cycles. The description of this methodology focuses primarily on the neutronics core simulator, and the methods described include the 2-D/1-D iterative scheme for solving the transport equation efficiently for the whole core. The depletion capabilities are also summarized, as is the coupling to CTF for T-H feedback. Implementation of these methods into the functionality necessary for PWR cycle depletion is demonstrated using Watts Bar Unit 1 cycles 1 and 2. The comparison to measurements in this simulation show reasonable accuracy, and the observed differences provide specific guidance for areas of ongoing work to improve the accuracy, along with performance improvements to reduce the execution time for a full-cycle depletion. Work is also ongoing to add the specific functionality in VERA-CS necessary to address the principal CASL milestones such as the simulation of Chalk River unidentified deposits on fuel assemblies.⁴⁰

Acknowledgments

This research was supported by CASL (www.casl.gov), an Energy Innovation Hub (<http://www.energy.gov/hubs>) for Modeling and Simulation of Nuclear Reactors under DOE contract DE-AC05-00OR22725. This research made use of the resources of the High Performance Computing Center at Idaho National Laboratory, which is supported by the Office of Nuclear Energy of DOE under contract DE-AC07-05ID14517. This manuscript has been authored by UT-Battelle, LLC, under contract DE-AC05-00OR22725 with DOE.

References

1. Consortium for Advanced Simulation of Light Water Reactors (CASL) Web Site (2014); <http://www.casl.gov> (current as of Feb. 3, 2016).
2. MPACT TEAM, "MPACT Theory Manual v2.1.0," CASL-U-2015-1005-000, Consortium for Advanced Simulation of Light Water Reactors (Dec. 2015).
3. M. N. AVRAMOVA, "CTF: A Thermal Hydraulic Sub-Channel Code for LWR Transient Analyses, User's Manual," The Pennsylvania State University, Department of Nuclear Engineering (2009).
4. I. C. GAULD et al., "Isotopic Depletion and Decay Methods and Analysis Capabilities in SCALE," *Nucl. Technol.*, **174**, 169 (2011); <http://dx.doi.org/10.13182/NT11-3>.
5. K. SMITH and B. FORGET, "Challenges in the Development of High Fidelity LWR Core Neutronics Tools," *Proc. M&C 2013*, Sun Valley, Idaho, May 5–9, 2013, American Nuclear Society (2013).
6. A. T. GODFREY, "MPACT Testing and Benchmarking Results," CASL-U-2014-0045-000, Oak Ridge National Laboratory (2014); <http://www.casl.gov/docs/CASL-U-2014-0045-000.pdf> (current as of Feb. 3, 2016).
7. B. COLLINS et al., "Stability and Accuracy of 3D Neutron Transport Simulations Using the 2D/1D Method in MPACT," *J. Comp. Phys.*, **326**, 612 (2016); <http://dx.doi.org/10.1016/j.jcp.2016.08.022>.
8. H. G. JOO et al., "Methods and Performance of a Three-Dimensional Whole Core Transport Code DeCART," *Proc. PHYSOR 2004*, Chicago, Illinois, April 25–29, 2004, American Nuclear Society (2004).
9. N. Z. CHO, G. S. LEE, and C. J. PARK, "Fusion Method of Characteristics and Nodal Method for 3D Whole Core Transport Calculation," *Trans. Am. Nucl. Soc.*, **86**, 322 (2002).
10. F. FÉVOTTE and B. LATHUILIÈRE, "MICADO: Parallel Implementation of a 2D-1D Iterative Algorithm for the 3D Neutron Transport Problem in Prismatic Geometries," *Proc. M&C 2013*, Sun Valley, Idaho, May 5–9, 2013, American Nuclear Society (2013).
11. A. MARIN-LAFLECHE, M. A. SMITH, and C. LEE, "PROTEUS-MOC: A 3D Deterministic Solver Incorporating 2D Method of Characteristics," *Proc. M&C 2013*, Sun Valley, Idaho, May 5–9, 2013, American Nuclear Society (2013).
12. Y. S. JUNG et al., "Practical Numerical Reactor Employing Direct Whole Core Neutron Transport and Subchannel Thermal/Hydraulic Solvers," *Ann. Nucl. Energy*, **62**, 357 (2013); <http://dx.doi.org/10.1016/j.anucene.2013.06.031>.
13. M. J. HALSALL, "CACTUS, A Characteristics Solutions to the Neutron Transport Equations in Complicated Geometries," AEEW-R-1291, U.K. Atomic Energy Authority (1980).
14. B. KOCHUNAS, "A Hybrid Parallel Algorithm for the 3-D Method of Characteristics Solution of the Boltzmann Transport Equation on High Performance Compute Clusters," PhD Dissertation, University of Michigan (2013);

- <http://deepblue.lib.umich.edu/handle/2027.42/100072> (current as of Feb. 3, 2016).
15. S. STIMPSON, B. COLLINS, and T. DOWNAR, "Axial Transport Solvers for the 2D/1D Scheme in MPACT," *Proc. PHYSOR 2014*, Kyoto, Japan, September 28–October 3, 2014.
 16. H. FINNEMANN, F. BENNEWITZ, and M. WAGNER, "Interface Current Techniques for Multidimensional Reactor Calculations," *Atomkernenergie*, **30**, 123 (1977).
 17. B. KOCHUNAS et al., "Operational Reactor Depletion Analysis Capability," CASL-U-2014-0189-000, Consortium for Advanced Simulation of Light Water Reactors (2014).
 18. A. ZHU et al., "Assessment of the Depletion Capability in MPACT," *Proc. PHYSOR 2014*, Kyoto, Japan, September 28–October 3, 2014.
 19. K. S. KIM et al., "Development of a New 47-Group Library for the CASL Neutronics Simulators," *Proc. M&C, SNA & MC 2015*, Nashville, Tennessee, April 19–23, 2015, American Nuclear Society (2015).
 20. W. WIESELQUIST, "The SCALE 6.2 ORIGEN API for High Performance Depletion," *Proc. M&C, SNA & MC 2015*, Nashville, Tennessee, April 19–23, 2015, American Nuclear Society (2015).
 21. D. WIARDA et al., "AMPX-2000: A Cross-Section Processing System for Generating Nuclear Data for Criticality Safety Applications," *Proc. Int. Conf. Nuclear Criticality Safety (ICNC 2015)*, Charlotte, North Carolina, September 13–17, 2015, American Nuclear Society (2015).
 22. "SCALE, A Modular Code System for Performing Standardized Computer Analyses for Licensing Evaluation," ORNL-TM/2005/39, Version 6, Vols. I–III, Oak Ridge National Laboratory (2009).
 23. A. KHAIRALLAH and J. RECOLIN, "Calcul de l'auto-protection résonnante dans les cellules complexes par la méthode des sous-groupes," *Proc. Seminar IAEA-SM-154 on Numerical Reactor Calculations*, p. 305, International Atomic Energy Agency (1972).
 24. R. J. J. STAMM'LER et al., "The HELIOS Methods," Studsvik Scandpower (1998).
 25. S. G. HONG and K. S. KIM, "Iterative Resonance Treatment Methods Using Resonance Integral Table in Heterogeneous Transport Lattice Calculations," *Ann. Nucl. Energy*, **38**, 32 (2011); <http://dx.doi.org/10.1016/j.anucene.2010.08.022>.
 26. M. L. WILLIAMS and K. S. KIM, "The Embedded Self-Shielding Method," *Proc. PHYSOR 2012*, Knoxville, Tennessee, April 15–20, 2012, American Nuclear Society (2012).
 27. Y. LIU et al., "A Full-Core Resonance Self-Shielding Method Using a Continuous-Energy Quasi-One-Dimensional Slowing-Down Solution that Accounts for Temperature-Dependent Fuel Subregions and Resonance Interference," *Nucl. Sci. Eng.*, **180**, 247 (2015); <http://dx.doi.org/10.13182/NSE14-65>.
 28. R. GOLDSTEIN and E. R. COHEN, "Theory of Resonance Absorption of Neutrons," *Nucl. Sci. Eng.*, **13**, 132 (1962); <http://dx.doi.org/10.13182/NSE62-1>.
 29. Y. LIU et al., "Resonance Self-Shielding Methodology in MPACT," *Proc. M&C 2013*, Sun Valley, Idaho, May 5–9, 2013, American Nuclear Society (2013).
 30. C. A. WEMPLE et al., "Improved Temperature-Dependent Resonance Treatment in HELIOS-1.9," *Trans. Am. Nucl. Soc.*, **96**, 657 (2007).
 31. The HDF Group, Hierarchical Data Format, Version 5, 1997–2016; <https://www.hdfgroup.org/> (current as of Dec. 4, 2016).
 32. A. T. GODFREY, "VERA Core Physics Benchmark Progression Problem Specifications," CASL-U-2012-0131-004, Rev. 4, Oak Ridge National Laboratory (Aug. 29, 2014).
 33. M. TABUCHI et al., "Yet Another Optimum Polar Angle Quadrature Set for the Method of Characteristics," *Trans. Am. Nucl. Soc.*, **93**, 506 (2005).
 34. B. R. HERMAN et al., "Improved Diffusion Coefficients Generated From Monte Carlo Codes," *Proc. M&C 2013*, Sun Valley, Idaho, May 5–9, 2013, American Nuclear Society (2013).
 35. K. S. KIM, "Generation of the V4.2m1 AMPX and MPACT 51 and 252-Group Libraries with ENDF/B-VII.0 and VII.1," CASL-U-1177-000, Consortium for Advanced Simulation of Light Water Reactors (Sep. 16, 2016).
 36. S. STIMPSON et al., "Automation and Assessment of Fuel Temperature Tables Used by VERA-CS," CASL-X-2016-1203-000, Consortium for Advanced Simulation of Light Water Reactors (Sep. 30, 2016).
 37. R. WILLIAMSON et al., "Multidimensional Multiphysics Simulation of Nuclear Fuel Behavior," *J. Nucl. Mater.*, **423**, 149 (2012); <http://dx.doi.org/10.1016/j.jnucmat.2012.01.012>.
 38. D. GASTON et al., "MOOSE: A Parallel Computational Framework for Coupled Systems of Nonlinear Equations," *Nucl. Eng. Des.*, **239**, 1768 (2009); <http://dx.doi.org/10.1016/j.nuengdes.2009.05.021>.
 39. S. PALMTAG, "Investigation of Thermal Expansion Effects in MPACT," CASL-U-2016-1015-000, Consortium for Advanced Simulation of Light Water Reactors (Feb. 28, 2016).
 40. B. COLLINS et al., "Simulation of CRUD-Induced Power Shift Using the VERA Core Simulator and MAMBA," *Proc. PHYSOR 2016*, Sun Valley, Idaho, May 1–5, 2016, American Nuclear Society (2016).